EXHIBIT 5

Featured Article

Quantitative Analysis of Biomarkers Defines an Optimal Biological Dose for Recombinant Human Endostatin in Primary Human Tumors

Darren W. Davis,[1] Yu Shen,[2] Nizar A. Mullani,[6] Sijin Wen,[2] Roy S. Herbst,[3] Michael O'Reilly,[4] James L. Abbruzzese,[5] and David J. McConkey[1]

Departments of [1]Cancer Biology, [2]Biostatistics, [3]Thoracic/Head and Neck Medical Oncology, [4]Radiation Oncology, and [5]Gastrointestinal Medical Oncology, The University of Texas M. D. Anderson Cancer Center, Houston, Texas, and [6]Department of Diagnostic Imaging, The University of Texas-Houston Health Science Center, Houston, Texas

Abstract

Purpose: In a recent study, we presented preliminary evidence for biological activity in a Phase I dose-finding study ($15–600$ mg/m^2) of recombinant human endostatin in patients with refractory solid tumors. Here, we conducted additional biomarker analyses to correlate changes in tumor biology with dose.

Experimental Design: Excisional tumor biopsies were obtained at baseline and after 56 days of endostatin therapy. Laser scanning cytometry (LSC) was used to quantify biomarker levels in whole tissue sections. Apoptosis in tumor cells (TCs) and tumor-associated endothelial cells (ECs) was quantified by fluorescent three-color anti-CD31/terminal deoxynucleotidyl transferase-mediated nick end labeling staining. Microvessel densities were measured by LSC-guided vessel contouring. Levels of tumor-associated EC BCL-2 and hypoxia-inducible factor 1α were determined by immunofluorescence and LSC quantification. The results, including tumor blood flow measured by positron emission tomography, were analyzed using a quadratic polynomial model.

Results: Significant increases in EC death and decreases in tumor microvessel density were observed, with maximal effects of endostatin at a dose of 249 mg/m^2 (95% confidence interval, 159–338) and 257 mg/m^2 (95% confidence interval, 183–331), respectively. In contrast, levels of TC death were uniformly low and did not correlate with endostatin dose. Maximal nuclear hypoxia-inducible factor 1α and minimal EC Bcl-2 levels were observed at $\sim$250 mg/m^2, although the changes did not reach statistical significance.

Conclusions: The data suggest that endostatin had optimal biological activity at doses $\sim$250 mg/m^2 in our cohort of patients. Endostatin's failure to induce high levels of TC death may explain its lack of significant clinical activity in this Phase I trial.

Introduction

Angiogenesis is the dynamic process of new blood vessel formation from the established vasculature (1, 2). Angiogenesis occurs in physiological situations such as embryonic development and wound healing but is also critical for tumor progression and metastasis (3–5). Recent work has demonstrated that tumors often stimulate angiogenesis via production of factors (*e.g.,* vascular endothelial growth factor, basic fibroblast growth factor, interleukin 8) that promote endothelial cell (EC) proliferation, survival, and differentiation (5, 6), and overexpression of one or more of these factors often predicts poor prognosis (7). Importantly, the ECs that make up the tumor vasculature are considered functionally normal in that they do not appear to accumulate genetic defect(s) (8, 9). Therefore, tumor-associated ECs may not acquire a drug-resistant phenotype, making them an attractive target for therapeutic intervention (3, 5, 10).

Although targeting tumor-associated ECs offers conceptual advantages over conventional anticancer therapeutic strategies, new procedures may be required to effectively evaluate the effects of antiangiogenic agents in clinical trials (11). Preclinical single-agent studies indicate that these compounds are cytostatic rather than cytotoxic (12, 13). Therefore, antiangiogenic therapy may have little effect on tumor size in advanced disease but still may prove beneficial in long-term maintenance approaches in patients with minimal residual disease or when it is combined with conventional therapies in patients with bulky or metastatic disease. Ironically, the nontoxic properties of these agents create complications for clinical trial design (14–16). The maximum-tolerated dose is usually determined by the dose-limiting toxicity (incidence <33%), and it serves as the basis for the identification of an active dose range (17). However, because angiogenesis inhibitors often lack toxicity and their biological activities may not be related to their maximum-tolerated doses, defining their optimal biological doses may be essential to exploiting their full therapeutic potential (14).

Endostatin is a M_r 20,000 COOH-terminal cleavage frag-

Requests for reprints: David McConkey, Department of Cancer Biology–173, University of Texas M. D. Anderson Cancer Center, 1515 Holcombe Boulevard, Houston, Texas 77030. Phone: (713) 792-8591; Fax: (713) 792-8747; E-mail: dmcconke@mdanderson.org.

ment of collagen XVIII that can function as an endogenous inhibitor of angiogenesis (8, 18). Endostatin's receptor(s) has not been isolated, and its mechanism(s) of action remains obscure. Nonetheless, candidates include interference with vascular endothelial growth factor and/or basic fibroblast growth factor signaling (19), inhibition of EC proliferation (20), migration (20, 21) or adhesion (22), disruption of cytoskeletal organization (23), interference with vascular precursors, and inhibition of matrix metalloproteases (24). Irrespective of the immediate effects of endostatin action, several investigators have demonstrated that it down-regulates BCL-2 and induces apoptosis in ECs (24, 25), which most likely play major roles in its antiangiogenic effects.

To more directly evaluate endostatin's effects on human tumors, our institution carried out one of three National Cancer Institute-sponsored Phase I dose escalation trials (15–600 mg/m^2) of recombinant human endostatin (rh-Endo) in patients with advanced solid malignancies (26). The primary objective of our trial was to determine whether biological surrogates of drug activity could be identified using noninvasive and invasive strategies (27). To this end, patients enrolled in this trial were required to provide an excisional biopsy just before the initiation of rh-Endo therapy and a second after the completion of two courses of therapy (56 days; Ref. 27). In addition, tumor blood flow and glucose metabolism were measured by positron emission tomography (PET) in marker lesions that were in most cases distinct from the ones that were biopsied at baseline and after the first and second courses of therapy (27). Detailed descriptions of the trial design and preliminary results are provided elsewhere (26, 27). Importantly, although we were able to detect significant changes in several of the markers studied, no clear dose-response relationship was observed for any of them (27). Therefore, the present study was initiated to provide a more rigorous characterization of likely biomarkers of antiangiogenic activity. To gain more information about intratumoral heterogeneity, we performed additional measurements of cell death in tumor cells (TCs) and tumor-associated ECs, and we also conducted new experiments designed to test possible effects of endostatin on other parameters of angiogenesis inhibition. The results suggest that endostatin has measurable biological activity but that it is maximal at intermediate doses of the drug, ~250 mg/m^2.

Materials and Methods

Tumor Biopsies. The Phase I trial design, patient characteristics, doses, and schedule are described in detail elsewhere (26, 27). An excisional tissue biopsy was required at study entry and again at the end of the second cycle (56 days). Seventeen patients with pre- and posttreatment biopsies were included in the study. Tumor type and biopsy size, including the measurement of tumor blood flow by PET, were previously reported (27). The average number of cells analyzed in each biopsy was ~5,000. Tissues were washed in PBS, embedded in Tissue-Tek OCT (Miles, Inc., Elkhart, IN), and frozen immediately by slow freezing in liquid nitrogen for 1–2 min, then stored at −80°C.

Laser Scanning Cytometry (LSC) Detection of Immunofluorescence CD31 (ECs) and TUNEL (Terminal Deoxynucleotidyl Transferase dUTP Nick-End Labeling). Frozen biopsies were sectioned (8 μm), fixed with cold acetone for 5 min, and washed with PBS for 3 min. Tissues were incubated with 0.2% Triton X-100 in PBS for 5 min and then washed three times with PBS for 3 min. Tissues were incubated with protein block (5% normal horse serum in PBS) for 15 min. Protein block was removed, and tissues were incubated with a 1:400 dilution of monoclonal antihuman CD31 (clone JC/70A; Dako Corporation, Carpinteria, CA) in protein block overnight at 4°C. Avoiding exposure to light, tissues were washed with PBS three times for 3 min and incubated with a 1:200 dilution of Cy5-conjugated goat antimouse secondary (Jackson Immuno-Research Laboratories, West Grove, PA) in protein block for 4 h at 4°C. Tissues were incubated with 4% paraformaldehyde at room temperature for 10 min and washed twice with PBS for 5 min. Fluorescent TUNEL (Promega, Madison, WI) was performed by incubating tissues with reaction buffer (from kit) for 5 min and then reaction buffer containing all components from the kit in a humid atmosphere at 37°C for 1 h, avoiding exposure to light. Next, tissues were washed three times with PBS for 5 min each to remove unincorporated fluorescein-dUTP. Cell nuclei were counterstained with 1 μg/ml propidium iodide for 5 min. Tissues were then washed with PBS twice for 3 min, and Prolong (Molecular Probes, Eugene, OR) was used to mount coverslips.

Immunofluorescence microscopy was performed using an objective (×200; Zeiss Plan-Neofluar) on an epifluorescence microscope equipped with narrow bandpass excitation filters mounted in a filter wheel to select for green and red fluorescence. Images were captured using a chilled CCD camera (Hamamatsu) on a PC computer and were processed using Adobe PhotoShop software (Adobe Systems, Mountain View, CA).

Three-color immunofluorescence analysis of CD31 and TUNEL was quantified by LSC (CompuCyte Corporation, Cambridge, MA) as described previously (27–29). The LSC is an instrument designed to enable fluorescence-based quantitative measurements on cellular preparations at the single cell level. The instrument consists of a base unit containing an Olympus BX50 fluorescent microscope and an optics unit coupled to an Argon and HeNe laser. Biopsies were carefully evaluated for the quality of immunofluorescent staining before LSC analysis. Each slide was placed on a computer-controlled motorized stage, and the desired area to be scanned was visually located using the instrument's epifluorescent microscope, excluding normal tissue and necrotic regions. The LSC was used very much like a fluorescent activated cell sorter to obtain two- and three-color fluorescent intensity information from the heterogeneous tissue specimens. Slides were scanned using a ×20 objective, and cell nuclei were contoured using the red fluorescence (propidium iodide) detector. The threshold contour was set to optimize cellular contours. CD31-positive cells were detected by Cy5 fluorescence using the long-red fluorescence detector, and TUNEL-positive events were detected using the green detector. The relative levels of fluorescence for each cell were plotted on a scattergram. The analytical gates define four quadrants that determine the total number of cells within each

population (CD31⁻/TUNEL⁺, CD31⁺/TUNEL⁺, and so forth). Each gate was set based on the fluorescent properties of the negative control sample (secondary antibody). The relocation feature was used to confirm TUNEL-positive and CD31-positive cells. Each data file was replayed to determine the percentages of apoptotic tumor-associated ECs and TCs in each biopsy.

LSC Analysis of Tumor Microvessels. Immunofluorescence detection of microvessels was achieved by staining with anti-CD31 according to the previous protocol. After coverslips were mounted, tissues were scanned by LSC. Each slide was placed on a computer-controlled motorized stage, and the desired area to be scanned was visually located using the instrument's epifluorescent microscope, excluding normal tissue and necrotic regions. Slides were scanned using a ×20 objective, and microvessels were contoured using the long-red fluorescence detector. The threshold contour was set to optimize microvessel contours based on contiguous fluorescence of Cy-5 (CD31). A gate was set based on the fluorescent properties of the negative control sample (secondary antibody). Each microvessel contoured was plotted on a x and y coordinate position map, and the total number of microvessels was recorded in the region statistics. The total number of microvessels was determined for each biopsy, and microvessel density (MVD) was calculated by taking the ratio of microvessels to the total number of cells in the same region obtained from analyzing CD31 and TUNEL.

Immunofluorscence Detection and LSC Analysis of Bcl-2/Hypoxia-Inducible Factor 1α (HIF-1α). For EC Bcl-2 detection, anti-CD31 staining was performed according to the previous protocol. After staining for CD31, tissues were washed twice with PBS containing 0.1% Brij for 3 min and washed once with PBS for 3 min. Tissues were then incubated with monoclonal antihuman Bcl-2 oncoprotein (clone 124; Dako Corporation) in protein block overnight at 4°C. Avoiding exposure to light, tissues were washed with PBS three times for 3 min and incubated with a 1:600 dilution of FITC-conjugated goat antimouse secondary (Jackson ImmunoResearch Laboratories) in protein block for 4 h at 4°C. Tissues were washed twice with PBS containing 0.1% Brij for 3 min and washed once with PBS for 3 min. Cell nuclei were counterstained with 1 μg/ml propidium iodide for 5 min. Tissues were then washed with PBS twice for 3 min, and Prolong (Molecular Probes) was used to mount coverslips.

For HIF-1α detection, frozen biopsies were sectioned (8 μm), fixed with cold acetone for 5 min, and washed with PBS for 3 min. Tissues were incubated with 0.2% Triton X-100 in PBS for 5 min and then washed three times with PBS for 3 min. Next, tissues were incubated with protein block (5% normal horse serum in PBS) for 15 min. Protein block was removed and tissues were incubated with a 1:100 dilution of monoclonal antihuman anti-HIF-1α monoclonal IgG 2b (clone H1α67; Novus Biologicals, Littleton, CO) in protein block overnight at 4°C. Avoiding exposure to light, tissues were washed with PBS three times for 3 min and incubated with a 1:200 dilution of Cy5-conjugated goat antimouse secondary in protein block for 4 h at 4°C. Tissues were washed twice with PBS containing 0.1% Brij for 3 min. For LSC analysis, cell nuclei were counterstained with 1 μg/ml propidium iodide for 5 min. Alternatively, 1 μg/ml sytox (Molecular Probes) was used to visualize cell nuclei for colocalization of nuclear translocation of HIF-1α.

Table 1 Summary of *adjusted*-R^2 from linear and quadratic models

	Linear	With quadratic
Apoptotic endothelial cell	0.066	0.262
Apoptotic tumor cell	0.006	00.0
Microvessel density	0.056	0.318
Flow	0.16	0.485
Hypoxia-inducible factor-1α	0.015	0.017

Tissues were then washed with PBS twice for 3 min, and Prolong (Molecular Probes) was used to mount coverslips.

For LSC quantification, slides were scanned using a ×20 objective, and cell nuclei were contoured using the red fluorescence (propidium iodide) detector. The threshold contour was set to optimize cellular contours. Bcl-2-positive cells were detected by FITC fluorescence using the green detector and HIF-1α-positive cells were detected by Cy5 fluorescence using the long-red detector. For HIF-1α nuclear expression levels, the LSC perimeter contour feature was selected. The relative levels of fluorescence for each cell were plotted on a scattergram. The analytical gates define four quadrants that determine the total number of cells within each population (CD31⁻/Bcl-2⁺, CD31⁺/Bcl-2⁺, and so forth). Each gate was set based on the fluorescent properties of the negative control sample (secondary antibody). The relocation feature was used to confirm Bcl-2 and HIF-1α-positive cells, and each data file was replayed to determine the percentages of each cell population.

Statistical Analysis. Mathematical criteria for fit were used to select the linear quadratic regression model for the analysis of data included in this study. The scatter plots of change *versus* rh-Endo dose observed with the results from analysis of apoptotic ECs and MVD measurements revealed a nonlinear pattern (unimodal). In particular, there was one peak dose value (maximum or minimum) of change for each variable. Graphical smoothing curves were used to examine the trends of the changes over dose using a nonparametric method, which indicated that a quadratic polynomial model would be appropriate to fit the data. Although the nonparametric method is flexible and does not depend upon the choice of the parametric curves, it is difficult to provide formal statistical inference from the model. Therefore, the quadratic polynomial model is specified for each variable while allowing for comparison of regression parameters between variables (Table 1). For each quadratic dose-response curve (biomarker change *versus* dose), we estimated the maximum or minimum change over rh-Endo dose. It was of interest to examine the dose level at which the maximum or minimum change occurred for each biomarker, and its 95% confidence interval (CI). Comparison of the maximum (with respect to EC death) and minimum (with respect to MVD) provided the estimation of optimal biological dose.

The quadratic regression model assumed that Y (the expected change) would vary with dose according to the following: $Y_i = a + b \times dose_i + c \times dose_i^2$.

The maximum or minimum dose was determined by $-b/(2 \times c)$ in this model, and its variance was estimated by the Delta method (30), which allowed us to construct 95% CIs for the maximum or minimum doses. The quadratic model was also applied to the changes in tumor blood flow obtained for each
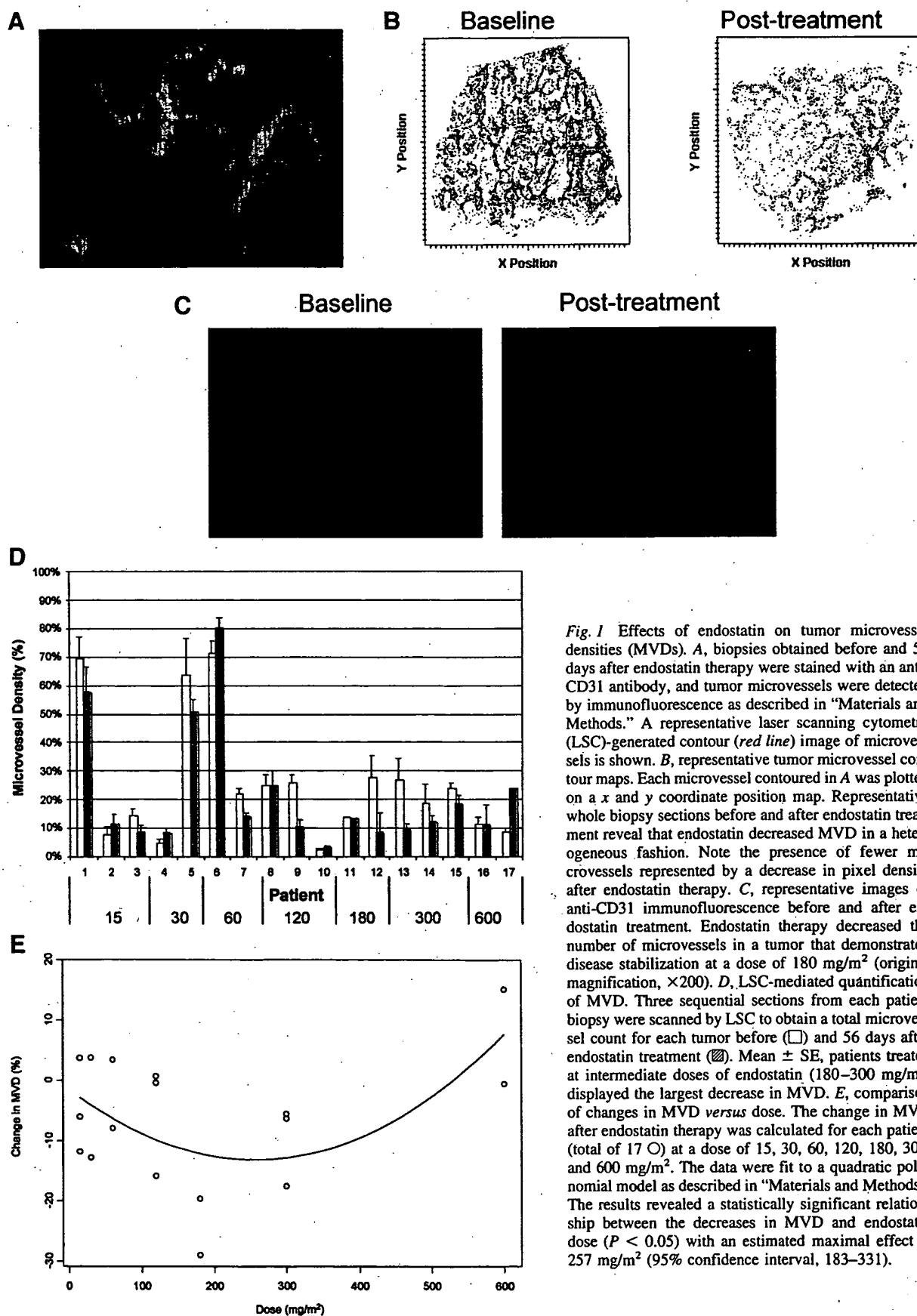
A

B Baseline   Post-treatment

C Baseline   Post-treatment

D

E

Fig. 1 Effects of endostatin on tumor microvessel densities (MVDs). *A*, biopsies obtained before and 56 days after endostatin therapy were stained with an anti-CD31 antibody, and tumor microvessels were detected by immunofluorescence as described in "Materials and Methods." A representative laser scanning cytometry (LSC)-generated contour (*red line*) image of microvessels is shown. *B*, representative tumor microvessel contour maps. Each microvessel contoured in *A* was plotted on a *x* and *y* coordinate position map. Representative whole biopsy sections before and after endostatin treatment reveal that endostatin decreased MVD in a heterogeneous fashion. Note the presence of fewer microvessels represented by a decrease in pixel density after endostatin therapy. *C*, representative images of anti-CD31 immunofluorescence before and after endostatin treatment. Endostatin therapy decreased the number of microvessels in a tumor that demonstrated disease stabilization at a dose of 180 mg/m^2 (original magnification, ×200). *D*, LSC-mediated quantification of MVD. Three sequential sections from each patient biopsy were scanned by LSC to obtain a total microvessel count for each tumor before (□) and 56 days after endostatin treatment (▨). Mean ± SE, patients treated at intermediate doses of endostatin (180–300 mg/m^2) displayed the largest decrease in MVD. *E*, comparison of changes in MVD *versus* dose. The change in MVD after endostatin therapy was calculated for each patient (total of 17 ○) at a dose of 15, 30, 60, 120, 180, 300, and 600 mg/m^2. The data were fit to a quadratic polynomial model as described in "Materials and Methods." The results revealed a statistically significant relationship between the decreases in MVD and endostatin dose ($P < 0.05$) with an estimated maximal effect at 257 mg/m^2 (95% confidence interval, 183–331).

patient (no blood flow data were obtained for patients at the 15 mg/m² dose level).

We compared the results obtained with the quadratic model with results obtained with a linear model via the use of *adjusted*-R² (Table 1). The squared multiple correlation coefficient, R², is the percentage of the variability in the dependent variables (*e.g.*, apoptotic EC) that could be explained by dose using a predictive equation. The *adjusted*-R² incorporates the degrees of freedom in the equation (*e.g.*, the degree of freedom is 1 for a linear model and 2 for a quadratic model). The value of *adjusted*-R² is between 0 and 1, and a larger value indicates a better fit (31). The values of *adjusted*-R² obtained from the linear and quadratic regression models are presented in Table 1, which shows that the quadratic models are better for apoptotic EC, MVD, or flow than the linear models, whereas linear models may fit equally well for analysis of the apoptotic TC or HIF-1α data.

Results

Effects of Endostatin on MVD. Antiangiogenic agents have been shown to reduce the number of tumor-associated microvessels in preclinical studies involving human tumor xenografts (8, 18). Therefore, to obtain a more direct measure of endostatin's potential antiangiogenic activity, we measured tumor MVDs by anti-CD31 immunofluorescence and LSC-guided contouring (Fig. 1A). Contiguous anti-CD31 immunofluorescence was used to generate MVD contour maps that revealed the numbers and locations of all blood vessels within each tumor biopsy section (Fig. 1B). Qualitative assessment of anti-CD31 immunofluorescence and MVD contour maps revealed a heterogeneous decrease in microvessels after endostatin therapy in some of the biopsy pairs (Fig. 1, B and C). LSC-mediated quantification was then used to obtain data from three sequential sections of each biopsy, excluding necrotic and normal tissue regions (Fig. 1D). Visual inspection of the changes in MVD revealed a nonlinear pattern, which suggested that a quadratic polynomial model would best fit the data (see "Materials and Methods"). Analysis of the results using this model revealed a significant relationship between MVD and dose of endostatin, with maximal effects estimated at 257 mg/m² (95% CI, 183–331; Fig. 1E, Table 2).

Effects of Endostatin on EC Death. In our previous study, we stained the tumor tissue sections obtained in this clinical trial by three-color immunofluorescence for detection of total cell nuclei, anti-CD31, and TUNEL, which allowed us to identify dying tumor-associated ECs and dying TCs within the same tissue section (27). We assigned a value to each biopsy based on the average level of cell death observed across the whole tumor section. However, a major concern that emerged was that the levels of cell death were extremely low, and potential problems in intratumoral heterogeneity (slide-to-slide variation) might make it impossible to obtain meaningful values from such studies. Therefore, to obtain a clearer picture of heterogeneity and, more importantly, to discern clear patterns of cell death, we performed additional staining to allow us to quantify levels of cell death in three independent regions (~1000 cells/region) within each of three sequential tissue sections cut from each biopsy and included some of the original data in the reanalysis. Analysis of the raw data confirmed that levels of cell death were markedly heterogeneous among the patient population, although intratumoral heterogeneity (represented by the error bars) was manageable (Fig. 2, A and B). Intriguingly, tumors from patients treated at intermediate doses of endostatin displayed significant increases in EC apoptosis (Fig. 2A).

Visual inspection of the changes in apoptosis revealed a nonlinear pattern, consistent with the changes in MVD (Fig. 1E). Therefore, we applied the quadratic polynomial model to the new data set to determine the relationships between levels of cell death and dose. These analyses revealed a significant relationship between endostatin dose and EC apoptosis (Fig. 2C, Table 2), with maximal effects at 249 mg/m² (95% CI, 159–338). However, levels of cell death within the CD31-negative (primarily TCs) compartment were not significantly associated with dose (Fig. 2D, Table 2), although TC death did correlate with EC death independently of dose (Pearson correlation coefficient = 0.6 with P = 0.01). The observation that maximal EC apoptosis and decreases in MVD were observed within the same range dose is consistent with the idea that the former causes the latter (12, 13, 32).

Effects of Endostatin on Bcl-2 and Nuclear HIF-1α Expression. Previous studies have implicated Bcl-2 in the maintenance of EC survival (33). Therefore, we investigated whether endostatin-induced apoptosis in tumor ECs was associated with decreased Bcl-2 expression. Excisional biopsies were stained by three-color immunofluorescence for detection of total cell nuclei, CD31 (ECs), and Bcl-2 (Fig. 3A). Fluorescence levels were subsequently quantified by LSC-mediated

Table 2 Estimation of parameters and maximum or minimum dose of endostatin

Estimation for the regression parameters was calculated for apoptotic endothelial cells (ECs) and tumor cells (TCs), microvessel density (MVD), tumor blood flow (flow), and hypoxia-inducible factor 1α (HIF-1α) using the model: $Y_i = a + b*dose + c*dose_i^2$. Parameters with (^{a}) are significant at a level of $P < 0.05$. The maximum (max) or minimum (min) dose with the 95% confidence interval (CI) was determined by $-b/(2*c)$ and was calculated by the Delta method (see "Materials and Methods"). These results yielded very similar max or min doses for apoptotic ECs and MVD with relatively narrow 95% CIs. Changes in tumor blood flow were significantly related to recombinant human endostatin dose, and the 95% CI overlapped considerably with those obtained for apoptotic ECs and MVD. In contrast, the very broad 95% CI obtained with quadratic analysis of TC death identified no max or min dose, indicating that there was no apparent relationship between TC death and endostatin dose.

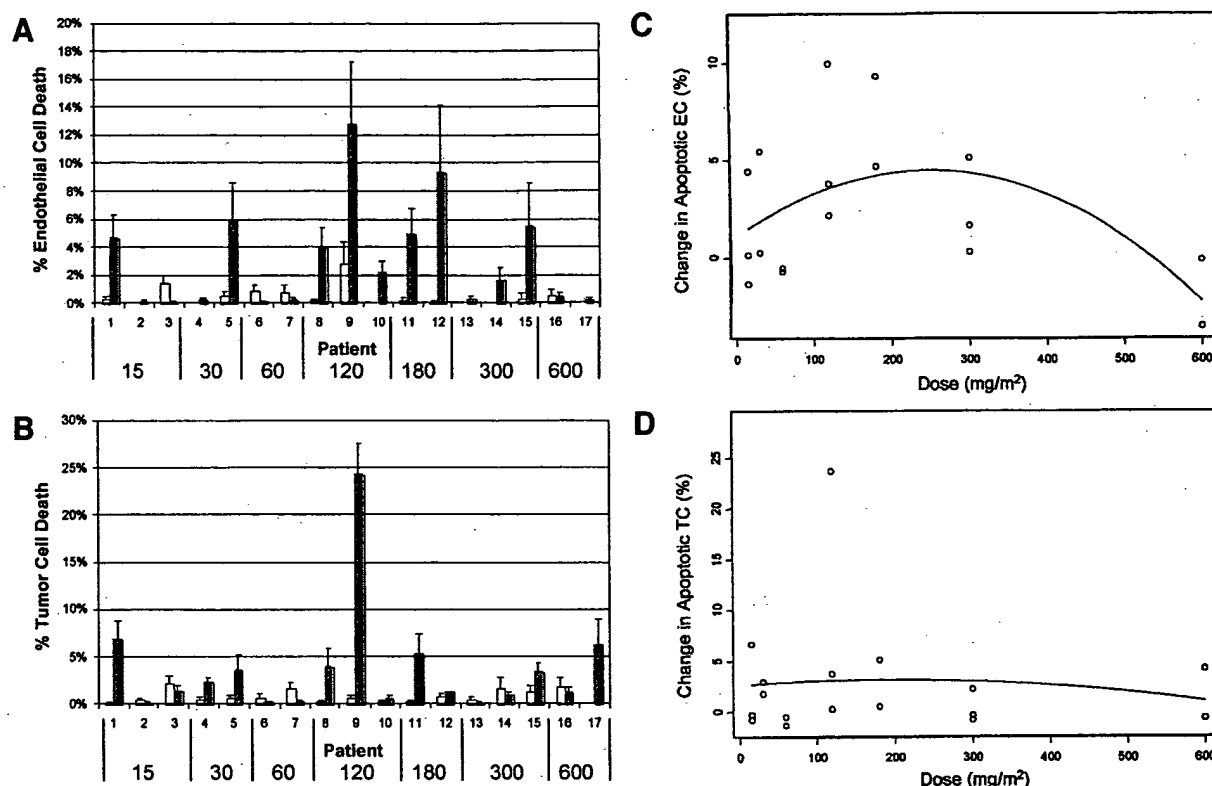| Parameter estimation	Apoptotic EC	Apoptotic TC	MVD	Flow	HIF-1α
a (SE)	0.011 (0.015)	0.026 (0.028)	−0.016 (0.042)	0.596 (0.202)	0.282 (0.469)
b (SE)	0.27 (0.150)^a	0.05 (0.28)	−0.908 (0.422)^a	−0.56 (0.166)^a	3.80 (4.731)
c (SE)	−0.546 (0.246)^a	−0.129 (0.046)	1.77 (0.680)^a	0.08 (0.028)^a	−7.53 (7.667)
Max-min dose (95% CI)	249 (159, 338)	197 (0, 1139)	257 (183, 331)	357 (270, 432)	252 (54, 451)

Fig. 2 Effects of endostatin on endothelial cell (CD31⁺) and nonendothelial cell (CD31⁻) apoptosis. Levels of cell death were measured by laser scanning cytometry (LSC) in excisional biopsies obtained before (□) and after (▨) 56 days of treatment with endostatin as described in "Materials and Methods." *A*, endothelial cell death. Percentages of CD31-positive and terminal deoxynucleotidyl transferase-mediated nick end labeling-positive cells were determined in three sequential tumor sections using an LSC. Mean ± SE, note that the cluster of patients treated at intermediate doses of endostatin displayed the largest increases in endothelial cell death. Patient 9 demonstrated disease stabilization with gradual escalation of recombinant human endostatin to 300 mg/m². *B*, tumor cell death. Percentages of CD31-negative and terminal deoxynucleotidyl transferase-mediated nick end labeling-positive cells were quantified by LSC. Mean ± SE, histological examination of the tissues indicated that the vast majority of the CD31-negative cells were tumor cells. *C*, relationship between tumor-associated endothelial cell death and dose of endostatin. The change in endothelial cell apoptosis after endostatin therapy was calculated for each patient ($n = 17$, ○) at a dose of 15, 30, 60, 120, 180, 300, and 600 mg/m². The quadratic polynomial model was used to determine the relationship between the change in endothelial cell apoptosis and dose as described in "Materials and Methods." The results revealed a statistically significant relationship between the increases in tumor-associated endothelial cell apoptosis and endostatin dose ($P < 0.05$) with an estimated maximal effect at 249 mg/m² (95% confidence interval, 159–338). *D*, relationship between tumor cell (CD31⁻ cells) death and dose of endostatin. The change in tumor cell apoptosis after endostatin therapy was calculated for each patient ($n = 17$, ○) at a dose of 15, 30, 60, 120, 180, 300, and 600 mg/m². The data were fit to a quadratic polynomial model. The results revealed no significant relationship between the increases in tumor cell death and endostatin dose ($P = 0.4$).

analysis (Fig. 3*B*). Analysis of the data using the quadratic polynomial model identified 236 mg/m² as the dose of endostatin producing maximal decreases in EC BCL-2 expression (Fig. 3*C*). However, as a result of greater variability in the data identified by a broader confidence interval (95% CI, 74–397), the relationship was not statistically significant. Interestingly, we observed a modest increase in Bcl-2 levels within the CD31-negative (primarily TCs) compartment that also appeared to peak at intermediate doses of rh-Endo, ~218 mg/m² (Fig. 3*D*).

HIF-1α is an oxygen-sensitive transcription factor that regulates the expression of a variety of hypoxia-associated genes, including erythropoietin and vascular endothelial growth factor (34–36). We therefore measured HIF-1α expression and cytoplasmic *versus* nuclear localization as candidate surrogates of tumor hypoxia (Fig. 4*A*). LSC-mediated analysis demonstrated that there was no relationship between cytoplasmic HIF-1α levels and rh-Endo dose (Fig. 4*B*). However, nuclear

HIF-1α appeared to increase at intermediate endostatin doses with maximal effects at 252 mg/m² (Fig. 4*C*). The broad 95% CI observed (CI, 54–451; Table 1) indicated that endostatin's effects on HIF-1α were much weaker than its effects on EC death or MVD.

Effects of Endostatin on Tumor Blood Flow. In a recently published study, we reported the effects of endostatin on tumor blood flow and glucose metabolism measured by PET at 28 and 56 days after therapy (27). Interestingly, analysis of the data using piecewise linear regression revealed a transition point at ~180 mg/m². We reanalyzed the 56-day PET blood flow data using the quadratic polynomial model to determine whether the data fit the model. However, in contrast to our previous study (27), we only included the patients for which matched baseline and posttreatment biopsies were available. Importantly, in all cases the marker lesions analyzed by PET were distinct from those biopsied. The results of our analyses revealed a significant
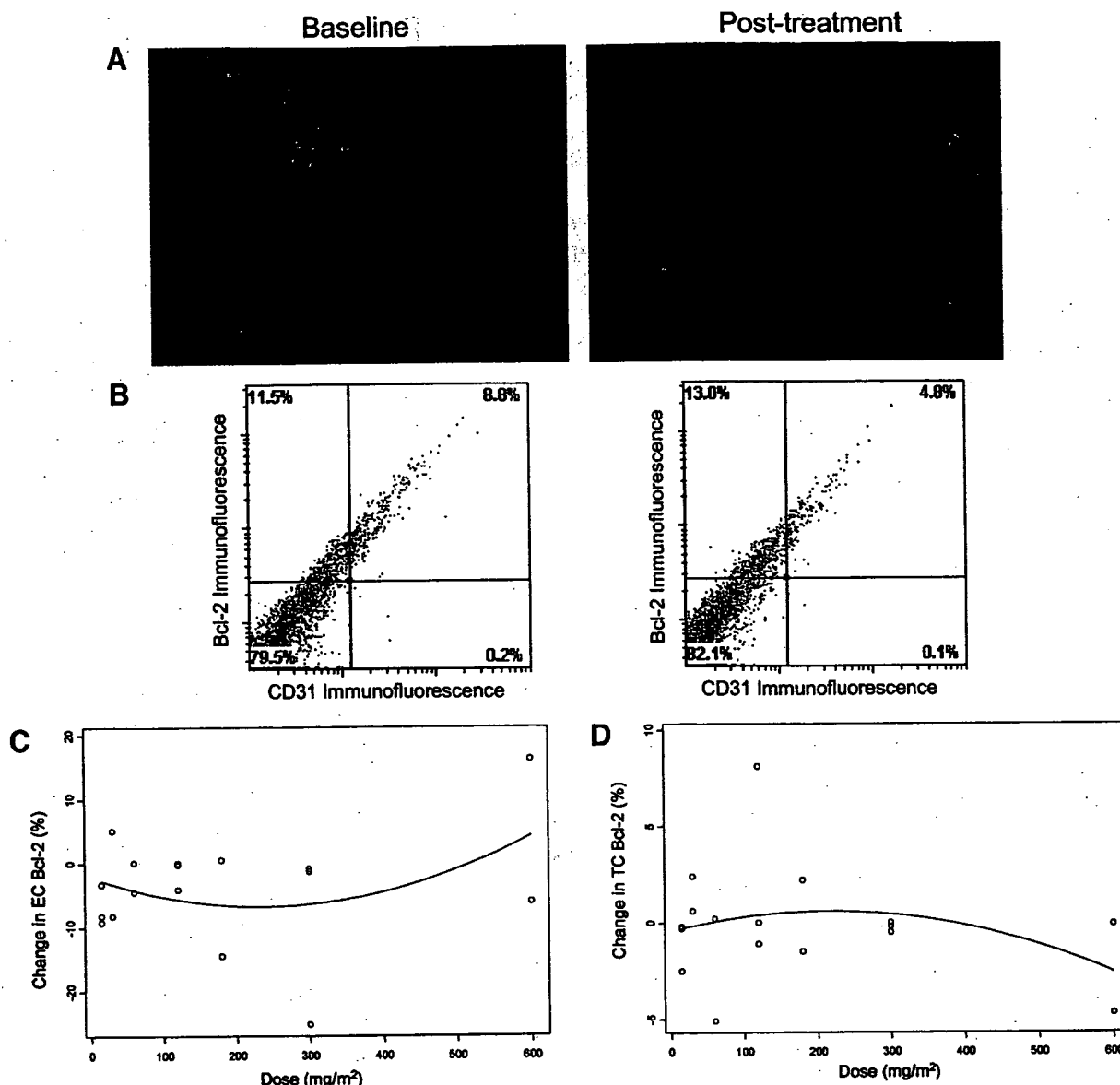
Fig. 3 Effects of endostatin on Bcl-2 expression. Levels of Bcl-2 were determined by laser scanning cytometry (LSC) in matched (pre- *versus* posttreatment) excisional biopsies obtained from 17 patients. *A*, immunofluorescent detection of BCL-2 in tumor cell subsets. Biopsies obtained before and 56 days after endostatin therapy were stained with antibodies specific for Bcl-2 and CD31 and counterstained with propidium iodide as described in "Materials and Methods." Representative images of Bcl-2 expression (*green*) and total cell nuclei (*red*) before and after endostatin treatment. *B*, quantitative analysis of BCL-2 expression by LSC. Representative LSC-generated scattergrams depicting the cellular changes in BCL-2 expression detected in the biopsies displayed in *A*. Each pixel in the scattergram corresponds to one cell in the biopsy sections. Note that in this particular tumor, the number of tumor-associated endothelial cells expressing Bcl-2 decreased from 8.8 to 4.8% (quadrant II) after endostatin treatment. *C*, relationship between changes in endothelial cell BCL-2 expression and dose. The change in endothelial cells expressing Bcl-2 was calculated for each patient (O) at a dose of 15, 30, 60, 120, 180, 300, and 600 mg/m². The quadratic polynomial model was used to correlate the changes observed with dose as described in "Materials and Methods." Although the change was not significant, a modest trend toward decreased BCL-2 expression was observed within the endothelial cell compartment, with maximal effects estimated at 236 mg/m² (95% confidence interval, 74–397). *D*, relationship between changes in tumor cell BCL-2 expression and dose. The change in tumor cells (CD31⁻) expressing Bcl-2 was calculated for each patient (O) at a dose of 15, 30, 60, 120, 180, 300, and 600 mg/m². The quadratic polynomial model was used to determine the relationship between the change in Bcl-2 expression and dose. Interestingly, a modest dose-related increase in BCL-2 expression was observed.

relationship between tumor blood flow and endostatin dose, with maximal effects estimated at 357 mg/m² (Fig. 5). The 95% CI overlapped considerably with those obtained in the measurements of EC apoptosis and MVD (95% CI, 270–432; Table 2).

Discussion

As more compounds targeting biological processes enter clinical trials in patients with cancer, it is becoming increasingly clear that a new paradigm for evaluating them must be devel-
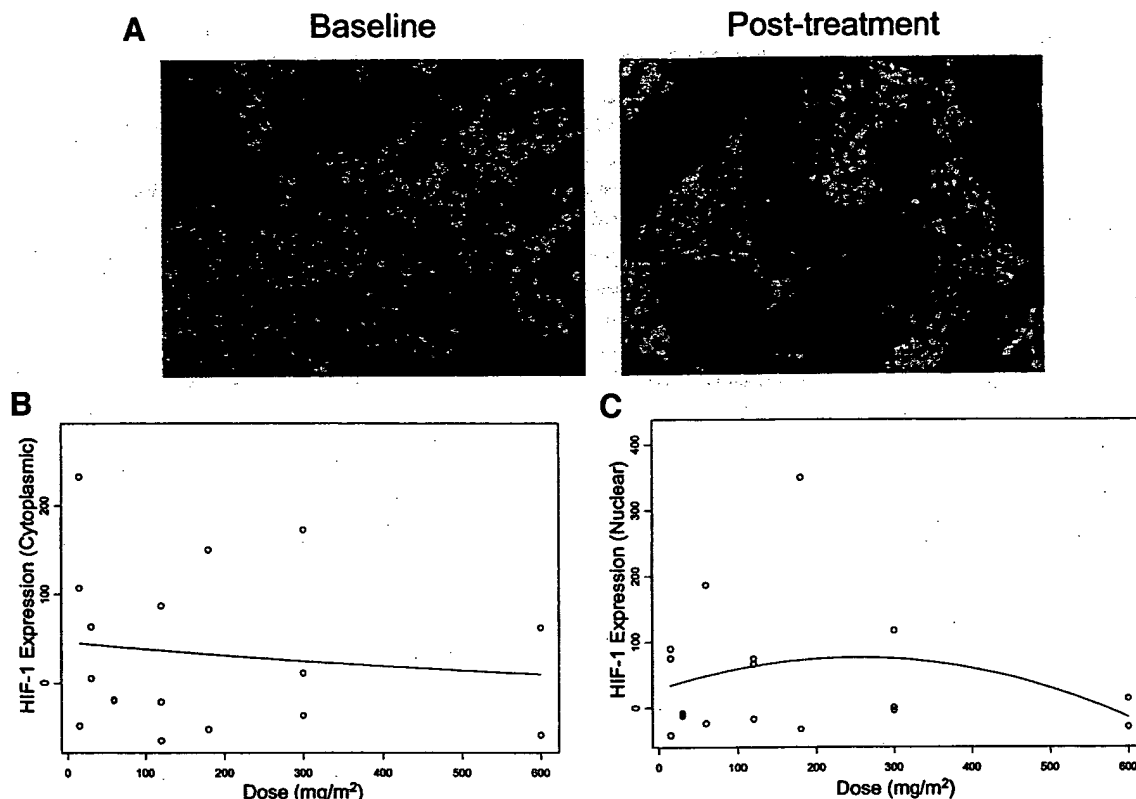
A **Baseline** **Post-treatment**

B

HIF-1 Expression (Cytoplasmic)

Dose (mg/m²)

C

HIF-1 Expression (Nuclear)

Dose (mg/m²)

Fig. 4 Analysis of hypoxia-inducible factor 1α (HIF-1α) expression. Levels of HIF-1α were determined in matched (pre *versus* post) excisional biopsies obtained from 17 patients as described in "Materials and Methods." *A*, immunofluorescent detection of HIF-1α. Biopsies were stained with an antibody specific for HIF-1α, and the polypeptide was detected by immunofluorescence (*red*) and the tissues were counterstained for total cell nuclei (*green*). Note that endostatin treatment induced nuclear localization of HIF-1α in this particular tumor, indicated by the intense *yellow staining* in the cell nuclei (red + green = yellow). *B*, effects of endostatin on total cellular HIF-1α. Tissue sections stained as shown in (*A*) were analyzed by LSC to determine the changes in protein expression in the cytoplasmic compartment of each cell. The change in cells expressing HIF-1α was calculated for each patient (O) at a dose of 15, 30, 60, 120, 180, 300, and 600 mg/m². The quadratic polynomial model was used to correlate the changes observed with dose as described in "Materials and Methods." Analysis of the data revealed no significant relationship between cytoplasmic HIF-1α expression and recombinant human endostatin dose. *C*, effects of endostatin on nuclear localization of HIF-1α. LSC was used to quantify colocalization of HIF-1α and propidium iodide staining, and the change in cells expressing HIF-1α was calculated for each patient (O) at a dose of 15, 30, 60, 120, 180, 300, and 600 mg/m². The data were evaluated using the quadratic polynomial model. Although the overall effects did not reach statistical significance, maximal nuclear HIF-1α localization was estimated at 252 mg/m² (95% confidence interval, 54–451 mg/m²).

oped if their biological activities are to be optimally exploited (11). Reports of direct tumor regression can be found in the published literature (8, 18), but most studies using biological agents have concluded that they are cytostatic rather than cyto-toxic. Furthermore, they appear to exhibit greater effects when overall tumor burden is low rather than in settings of bulky disease, and their maximal activities may not occur at their maximum-tolerated doses (11). These observations contrast sharply with what is observed with conventional cytotoxics (DNA damaging agents, taxanes, and so on), where the para-digm of identifying the maximum-tolerated dose as the basis for maximizing drug efficacy was developed (17, 37, 38).

In several collaborative preclinical studies, we demon-strated that tumor growth inhibition induced by different classes of biological agents that display antiangiogenic ac-tivity (IFNs, epidermal growth factor receptor antagonists, and VEGFR-2 receptor/KDR antagonists) is associated with increases in tumor EC apoptosis (12, 13, 32, 39). However, when we attempted to use manual counting methods to quan-

tify the effects of endostatin on EC death in the biopsies obtained in our clinical trial, it became immediately apparent that more objective and sensitive quantitative methods were required. This is, in part, because levels of EC death were very low, and our inability to discern clear patterns of cell death in these tissues by manual counting methods is con-sistent with the experience of another group that assessed the effects of endostatin in an independent Phase I trial (40). LSC analysis indicated that the average level of apoptosis in tumor-associated ECs was 0.2% before therapy and 1.1% after endostatin therapy, respectively (27). Although the ab-solute levels of cell death were extremely low, this actually represented a 5-fold increase in cell death, which is compa-rable with the fold increases observed in TC lines exposed to cytotoxic agents *in vitro*. Over time, this increase in cell death was probably sufficient to produce the decreases in MVD that were also observed in the tissues. It is possible that greater increases in cell death would have been observed had we sampled the tumors at a different (earlier) time point, but
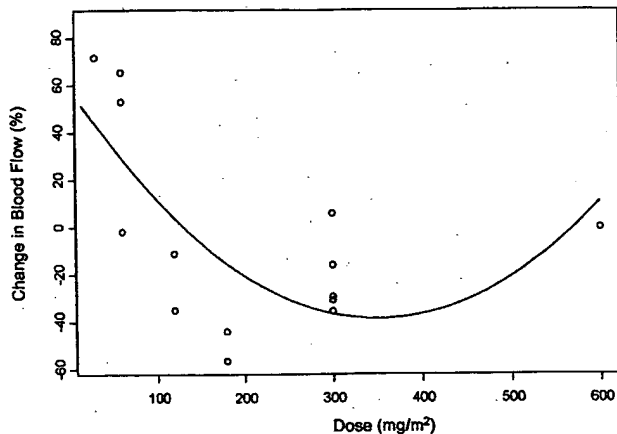
Fig. 5 Relationship between tumor blood flow and endostatin dose. Data were obtained from 14 of the 17 patients who provided baseline and posttreatment biopsies for the molecular analyses (no data were available for patients treated at the 15 mg/m² dose). The lesions imaged in all cases were different from those biopsied. The 56-day blood flow data obtained by positron emission tomography that was used in our previous study (29) were subjected to reanalysis using the quadratic polynomial model. The change in tumor blood flow was calculated for each patient (O) at a dose of 30, 60, 120, 180, 300, and 600 mg/m². The results revealed that endostatin significantly decreased tumor blood flow ($P < 0.05$), with maximal effects estimated at 357 mg/m² (95% confidence interval, 270–432 mg/m²). Note that data were available for only one patient at the 600 mg/m² dose level.

there were no empirical data available at the time this trial started to suggest when optimal effects would have been observed.

One of the intriguing findings made in the present study was that the changes in EC death and MVD were not linearly associated with dose of endostatin. Although we do not have a mechanistic explanation for these findings, it is possible that endostatin exerts its effects by interacting with surface receptor(s) that can be desensitized at supraoptimal concentrations of the polypeptide. Adoption of the quadratic polynomial model allowed us to identify the doses that produced maximal effects on the biological endpoints interrogated. Importantly, the dose of endostatin identified in each of these studies was very similar (~250 mg/m²). The effects were most striking when the results of the two most direct measures of antiangiogenic activity (MVD and EC apoptosis) were compared, where maximal effects were observed at 257 and 249 mg/m², respectively. Furthermore, Pairwise Pearson analysis confirmed that there was a strongly significant, inverse correlation between the two variables (correlation coefficient = −0.67 with $P = 0.003$). Reanalysis of the PET-based blood flow data also revealed that endostatin produced dose-related reductions, with maximal effects observed near the optimal biological dose identified in the other analyses. Although we do not have an explanation for why the blood flow measurements identified a somewhat higher optimal biological dose than the MVD or EC apoptosis analyses, it is possible that the fact that flow data were unavailable for the 15-mg/m² cohort caused a slight rightward shift in the dose-response curve.

Part of the data set used in the present study was previously reported elsewhere (27). However, several factors precluded us from proposing that endostatin produced dose-related effects on angiogenesis. First, percentages of apoptosis were averaged across whole biopsy sections without taking into account the potential intratumoral and technical heterogeneity associated with the samples. Our new analyses clearly display the variation associated with our measurements (Fig. 2). Even more important were the automated measurements of MVD, which served as independent (and statistically significant) indicators of biological effect. The nonlinear relationship between endostatin dose and response required that we analyze the data with a new statistical method (the quadratic polynomial model). Given the small number of patients enrolled at the critical dose levels, it is possible that the biology of the tumors (rather than endostatin itself) produced the changes in angiogenesis-related biomarkers measured here. We have attempted to confirm our results in preclinical studies in tumor xenografts, but limitations on drug availability have hampered these efforts, and it is conceivable that the effects of human endostatin on murine *versus* human ECs will differ. Unfortunately, although endostatin displayed some antitumor activity in two patients (stable disease, patient 9; partial regression of one lesion, patient 21), the drug did not produce any frank clinical responses. Hence, this work is hypothesis generating for future studies, although one would use these analyses to start the Phase II dose at 250 mg/m².

Finally, our data also provide a possible explanation for why we failed to observe significant clinical responses in our patient cohort. Although we observed a statistically significant relationship between EC death and TC death, the absolute levels of apoptosis reached in the TCs were modest at best and not comparable with the levels we observed in a previous study of the effects of neoadjuvant chemotherapy in breast cancer in which very significant clinical responses were obtained (28). Thus, we suspect that intrinsic tumor resistance to apoptosis contributed to endostatin's failure to produce significant clinical responses in our patient cohort (26) and the others (40, 41). Given that these patients were heavily pretreated with chemotherapeutic agents that probably act by inducing apoptosis (28), the emergence of intrinsic resistance is to be expected. Identifying the thresholds of EC and TC apoptosis required to produce direct antitumoral activity remains an important subject for ongoing investigation.

Acknowledgments

References

1. Folkman, J. Tumor angiogenesis. Adv. Cancer Res., *43:* 175–203, 1985.

2. Folkman, J. Angiogenesis in cancer, vascular, rheumatoid, and other disease. Nat. Med., *1:* 27–31, 1995.

3. Folkman, J. Tumor angiogenesis: therapeutic implications. N. Engl. J. Med., *285:* 1182–1186, 1971.

4. Weidner, N., Semple, J. P., Welch, W. R., and Folkman, J. Tumor angiogenesis and metastasis: correlation in invasive breast carcinoma. N. Engl. J. Med., *324:* 1–8, 1991.

5. Fidler, I. J., and Ellis, L. M. The implications of angiogenesis for the biology and therapy of cancer metastasis. Cell, *79:* 185–188, 1994.

6. Hanahan, D., and Folkman, J. Patterns and emerging mechanisms of the angiogenic switch during tumorigenesis. Cell, *86:* 353–364, 1996.

7. Relf, M., LeJeune, S., Scott, P. A., Fox, S., Smith, K., Leek, R., Moghaddam, A., Whitehouse, R., Bicknell, R., and Harris, A. L. Expression of the angiogenic factors vascular endothelial cell growth factor, acidic and basic fibroblast growth factor, tumor growth factor β-1, platelet-derived endothelial cell growth factor, placenta growth factor, and pleiotrophin in human primary breast cancer and its relation to angiogenesis. Cancer Res., *57:* 963–969, 1997.

8. Boehm, T., Folkman, J., Browder, T., and O'Reilly, M. S. Antiangiogenic therapy of experimental cancer does not induce acquired drug resistance. Nature (Lond.), *390:* 404–407, 1997.

9. Kerbel, R. S. A cancer therapy resistant to resistance. Nature (Lond.), *390:* 335–336, 1997.

10. Kerbel, R. S. Tumor angiogenesis: past, present and the near future. Carcinogenesis (Lond.), *21:* 505–515, 2000.

11. Davis, D. W., McConkey, D. J., Abbruzzese, J. L., and Herbst, R. S. Surrogate markers in antiangiogenesis clinical trials. Br. J. Cancer, *89:* 8–14, 2003.

12. Shaheen, R. M., Davis, D. W., Liu, W., Zebrowski, B. K., Wilson, M. R., Bucana, C. D., McConkey, D. J., McMahon, G., and Ellis, L. M. Antiangiogenic therapy targeting the tyrosine kinase receptor for vascular endothelial growth factor receptor inhibits the growth of colon cancer liver metastasis and induces tumor and endothelial cell apoptosis. Cancer Res., *59:* 5412–5416, 1999.

13. Bruns, C. J., Harbison, M. T., Davis, D. W., Portera, C. A., Tsan, R., McConkey, D. J., Evans, D. B., Abbruzzese, J. L., Hicklin, D. J., and Radinsky, R. Epidermal growth factor receptor blockade with C225 plus gemcitabine results in regression of human pancreatic carcinoma growing orthotopically in nude mice by antiangiogenic mechanisms. Clin. Cancer Res., *6:* 1936–1948, 2000.

14. Herbst, R. S., Lee, A. T., Tran, H. T., and Abbruzzese, J. L. Clinical studies of angiogenesis inhibitors: the University of Texas M. D. Anderson Center Trial of Human Endostatin. Curr. Oncol. Rep., *3:* 131–140, 2001.

15. Twardowski, P., and Gradishar, W. J. Clinical trials of antiangiogenic agents. Curr. Opin. Oncol., *9:* 584–589, 1997.

16. Eisenhauer, E. A. Phase I and II trials of novel anticancer agents: endpoints, efficacy and existentialism. The Michel Clavel Lecture, held at the 10th NCI-EORTC Conference on New Drugs in Cancer Therapy, Amsterdam, 16–19 June 1998. Ann. Oncol., *9:* 1047–1052, 1998.

17. Simon, R., Freidlin, B., Rubinstein, L., Arbuck, S. G., Collins, J., and Christian, M. C. Accelerated titration designs for Phase I clinical trials in oncology. J. Natl. Cancer Inst. (Bethesda), *89:* 1138–1147, 1997.

18. O'Reilly, M. S., Boehm, T., Shing, Y., Fukai, N., Vasios, G., Lane, W. S., Flynn, E., Birkhead, J. R., Olsen, B. R., and Folkman, J. Endostatin: an endogenous inhibitor of angiogenesis and tumor growth. Cell, *88:* 277–285, 1997.

19. Taddei, L., Chiarugi, P., Brogelli, L., Cirri, P., Magnelli, L., Raugei, G., Ziche, M., Granger, H. J., Chiarugi, V., and Ramponi, G. Inhibitory effect of full-length human endostatin on *in vitro* angiogenesis. Biochem. Biophys. Res. Commun., *263:* 340–345, 1999.

20. Yamaguchi, N., Anand-Apte, B., Lee, M., Sasaki, T., Fukai, N., Shapiro, R., Que, I., Lowik, C., Timpl, R., and Olsen, B. R. Endostatin inhibits VEGF-induced endothelial cell migration and tumor growth independently of zinc binding. EMBO J., *18:* 4414–4423, 1999.

21. Shichiri, M., and Hirata, Y. Antiangiogenesis signals by endostatin. FASEB J., *15:* 1044–1053, 2001.

22. Rehn, M., Veikkola, T., Kukk-Valdre, E., Nakamura, H., Ilmonen, M., Lombardo, C., Pihlajaniemi, T., Alitalo, K., and Vuori, K. Interaction of endostatin with integrins implicated in angiogenesis. Proc. Natl. Acad. Sci. USA, *98:* 1024–1029, 2001.

23. Dixelius, J., Larsson, H., Sasaki, T., Holmqvist, K., Lu, L., Engstrom, A., Timpl, R., Welsh, M., and Claesson-Welsh, L. Endostatin-induced tyrosine kinase signaling through the Shb adaptor protein regulates endothelial cell apoptosis. Blood, *95:* 3403–3411, 2000.

24. Kim, Y. M., Jang, J. W., Lee, O. H., Yeon, J., Choi, E. Y., Kim, K. W., Lee, S. T., and Kwon, Y. G. Endostatin inhibits endothelial and

tumor cellular invasion by blocking the activation and catalytic activity of matrix metalloproteinase. Cancer Res., *60:* 5410–5413, 2000.

25. Dhanabal, M., Ramchandran, R., Waterman, M. J., Lu, H., Knebelmann, B., Segal, M., and Sukhatme, V. P. Endostatin induces endothelial cell apoptosis. J. Biol. Chem., *274:* 11721–11726, 1999.

26. Herbst, R. S., Hess, K. R., Tran, H. T., Tseng, J. E., Mullani, N. A., Charnsangavej, C., Madden, T., Davis, D. W., McConkey, D. J., O'Reilly, M. S., Ellis, L. M., Pluda, J., Hong, W. K., and Abbruzzese, J. L. Phase I Study of recombinant human endostatin in patients with advanced solid tumors. J. Clin. Oncol., *20:* 3792–3803, 2002.

27. Herbst, R. S., Mullani, N. A., Davis, D. W., Hess, K. R., McConkey, D. J., Charnsangavej, C., O'Reilly, M. S., Kim, H. W., Baker, C., Roach, J., Ellis, L. M., Rashid, A., Pluda, J., Bucana, C., Madden, T. L., Tran, H. T., and Abbruzzese, J. L. Development of biologic markers of response and assessment of antiangiogenic activity in a clinical trial of human recombinant endostatin. J. Clin. Oncol., *20:* 3804–3814, 2002.

28. Davis, D. W., Buchholz, T. A., Hess, K. R., Sahin, A. A., Valero, V., and McConkey, D. J. Automated quantification of apoptosis after neoadjuvant chemotherapy for breast cancer: early assessment predicts clinical response. Clin. Cancer Res., *9:* 955–960, 2003.

29. Davis, D. W., Weidner, D. A., Holian, A., and McConkey, D. J. Nitric oxide-dependent activation of p53 suppresses bleomycin-induced apoptosis in the lung. J. Exp. Med., *192:* 857–869, 2000.

30. Agresti, A., and Min, Y. On small-sample confidence intervals for parameters in discrete distributions. Biometrics, *57:* 963–971, 2001.

31. Fisher, L. D. Biostatics: A Methodology for Health Sciences. New York: John Wiley & Sons, 1993.

32. Inoue, K., Slaton, J. W., Davis, D. W., Hicklin, D. J., McConkey, D. J., Karashima, T., Radinsky, R., and Dinney, C. P. Treatment of human metastatic transitional cell carcinoma of the bladder in a murine model with the anti-vascular endothelial growth factor receptor monoclonal antibody DC101 and paclitaxel. Clin. Cancer Res., *6:* 2635–2643, 2000.

33. Nor, J. E., Christensen, J., Mooney, D. J., and Polverini, P. J. Vascular endothelial growth factor (VEGF)-mediated angiogenesis is associated with enhanced endothelial cell survival and induction of Bcl-2 expression. Am. J. Pathol., *154:* 375–384, 1999.

34. Carmeliet, P., Dor, Y., Herbert, J. M., Fukumura, D., Brusselmans, K., Dewerchin, M., Neeman, M., Bono, F., Abramovitch, R., Maxwell, P., Koch, C. J., Ratcliffe, P., Moons, L., Jain, R. K., Collen, D., and Keshet, E. Role of HIF-1α in hypoxia-mediated apoptosis, cell proliferation, and angiogenesis. Nature (Lond.), *394:* 485–490, 1998.

35. Semenza, G. L., Agani, F., Feldser, D., Iyer, N., Kotch, L., Laughner, E., and Yu, A. Hypoxia, HIF-1, and the pathophysiology of common human diseases. Adv. Exp. Med. Biol., *475:* 123–130, 2000.

36. Semenza, G. L. HIF-1: using two hands to flip the angiogenic switch. Cancer Metastasis Rev., *19:* 59–65, 2000.

37. Storer, B. E. Design and analysis of Phase I clinical trials. Biometrics, *45:* 925–937, 1989.

38. Goodman, S. N., Zahurak, M. L., and Piantadosi, S. Some practical improvements in the continual reassessment method for Phase I studies. Stat. Med., *14:* 1149–1161, 1995.

39. Ozawa, S., Shinohara, H., Kanayama, H. O., Bruns, C. J., Bucana, C. D., Ellis, L. M., Davis, D. W., and Fidler, I. J. Suppression of angiogenesis and therapy of human colon cancer liver metastasis by systemic administration of interferon α. Neoplasia, *3:* 154–164, 2001.

40. Mundhenke, C., Thomas, J. P., Wilding, G., Lee, F. T., Kelzc, F., Chappell, R., Neider, R., Sebree, L. A., and Friedl, A. Tissue examination to monitor antiangiogenic therapy: a Phase I clinical trial with endostatin. Clin. Cancer Res., *7:* 3366–3374, 2001.

41. Eder, J. P., Jr., Supko, J. G., Clark, J. W., Puchalski, T. A., Garcia-Carbonero, R., Ryan, D. P., Shulman, L. N., Proper, J., Kirvan, M., Rattner, B., Connors, S., Keogan, M. T., Janicek, M. J., Fogler, W. E., Schnipper, L., Kinchla, N., Sidor, C., Phillips, E., Folkman, J., and Kufe, D. W. Phase I clinical trial of recombinant human endostatin administered as a short intravenous infusion repeated daily. J. Clin. Oncol., *20:* 3772–3784, 2002.